Journal of Volcanology and Geothermal Research 439 (2023) 107830

Contents lists available at ScienceDirect

Journal of Volcanology and Geothermal Research

journal homepage: www.journals.elsevier.com/journal-of-volcanology-and-geothermal-research

Deep and shallow crustal structure control on the late-stage volcanism in Syria Planum (Mars)

Riccardo Pozzobon [a], Francesco Mazzarini [b,*], Ilaria Isola [b]

[a] Dipartimento di Geoscienze, Università degli Studi di Padova, Italy
[b] Istituto Nazionale di Geofisica e Vulcanologia, Pisa, Italy

ARTICLE INFO

Keywords:
Volcanic vents clustering
Vent spatial distribution
Plumbing system
Structural inheritance
Mars

ABSTRACT

Long-lasting widespread volcanism in Mars is testified by the Tharsis volcanic province, one of the largest volcanic provinces with the largest shield volcanoes of the Solar System. However, volcanism on Mars is characterized also by the occurrence of broad volcanic fields, either in the form of small lava shields or monogenic volcanic cones. The region of Syria Planum (SP) is located east of the Tharsis province and between Noctis Labyrinthus to the North and Claritas Fossae to the southwest. It is an example of diffuse volcanism, presenting hundreds of small edifices (namely Syria Colles) which occur on top of a large bulge roughly 300 km × 200 km in size. SP exhibits a complex magmatic and volcano-tectonic evolution spanning from the early-Noachian to the more recent Amazonian. In this work, we investigate the geometry of the plumbing system of the SP volcanic field as well as the geometries of the volcanic constructs (i.e., vent elongation and vent alignment) that may be linked to the structures that fed the magma presenting a possible tectonic and volcanic evolution of the distributed volcanism phase in this area. The spatial distribution of vents and the overall map view shape of the volcanic field were studied in terms of vent clustering and spatial distribution. We show that the widespread and diffuse volcanism in SP presents clear vent clusters that are related to a deep source magma reservoir located at ~100 km depth. We also show that Syria Colles vent elongations and azimuth distributions suggest that the magma exploited the inherited regional structural framework, coherent with the Syria Colles late-stage Amazonian magmatic event, and highlighting the role of a shallow crustal tectonic framework in shaping the Martian volcanism.

1. Introduction

Syria Planum and the associated volcanism occur on a broader volcanic area known as Tharsis rise, one of the largest volcanic provinces of the Solar System including five large lava shields and another 12 smaller edifices (Baptista et al., 2008; Hauber et al., 2009; Richardson et al., 2013) including small lava shields, and tholuses related to both effusive and explosive activity (Brož and Hauber, 2012; Plescia, 2000). Throughout the years the increasing amount of images and topography datasets with high spatial and spectral resolution have allowed to define model ages from crater counting for all the volcanic constructs in the Tharsis Rise (Neukum et al., 2004; Werner, 2009; Robbins et al., 2011). These new chronological results reveal a complex volcano-tectonic evolution and magmatic history of the area spanning from the early-Noachian to the more recent volcanism such as the 130 Ma Arsia Mons' single caldera and the 140 Ma Pavonis Mons' composite calderas (Werner, 2009; Neukum et al., 2004; Pozzobon et al., 2015; Robbins et al., 2011; Pozzobon et al., 2021). Although through the years Syria Planum has been considered the by-product of the enormous volcano-tectonic activity forming the Tharsis rise (Anderson et al., 2004; Hiesinger et al., 2007; Baptista et al., 2008) it has been shown that this volcanic area could be related to large multiple episodes of mantle upwelling forming minor edifices that do not necessarily overlap with the major volcanic centres (Richardson et al., 2013, 2021; Greeley, 1977; Mège and Masson, 1996; Wilson and Head, 2002; Anderson et al., 2004). Moreover, the NW-SE elongated Syria Planum volcanic field occurs south of the Noctis Labyrinthus canyon systems that form a dissected highland (Bistacchi et al., 2004; Kling et al., 2021) and is located at the western tip of the Valles Marineris (Fig. 1).

In the ~4000 km-long WNW–ESE-trending subparallel troughs system forming the Valles Marineris, Amazonian volcanism is reported in one of its segments (Brustel et al., 2017; Brož et al., 2017). The large left

* Corresponding author at: Istituto Nazionale di Geofisica e Vulcanologia, Via Cesare Battisti, 53, 56125 Pisa, Italy.
E-mail address: francesco.mazzarini@ingv.it (F. Mazzarini).

https://doi.org/10.1016/j.jvolgeores.2023.107830
Received 3 March 2023; Received in revised form 17 May 2023; Accepted 2 June 2023
Available online 7 June 2023

lateral strike slip offset along the southern faults of Valles Marineris may have caused possible E-W extension in Noctis Labyrinthus and Syria Planum (Yin, 2012).

In this work, we investigate the depth of the plumbing system of the dispersed late–stage volcanism in Syria Planum as well as the geometries of the volcanic constructs (i.e., vent elongation and vents alignment) linked to the structures that fed the magma in order to forward a possible tectonic and volcanic evolution of the area. The spatial distribution of vents and the overall shape of the volcanic field have been studied in terms of vent clustering and spatial distribution. Moreover, analyzing the lineament pattern on Syria Planum and surrounding areas, structural links with the formation and evolution of the Noctis Labyrinthus graben, the Valles Marineris and the Tharsis province are forwarded.

2. Data set

An extensive dataset with sufficient resolution for identifying the local morphologies of volcanic features in Syria Planum has been used. In order to obtain this dataset, we combined a reference base map made of the MOLA (Mars Orbiter Laser Altimeter onboard Mars Global Surveyor) gridded data (Smith et al., 2001) at 463 m/pixel resolution and a THEMIS daytime IR global mosaic at 100 m/pixel resolution (Edwards et al., 2011; Table 1).

We cross-checked the presence of additional volcanic centres with respect to the existing mapping by means of HRSC (High Resolution Stereo Camera, Neukum et al., 2004; Jaumann et al., 2007) ND4 nadir images and DA4 DTMs (Digital Terrain Models, level 4 data products comparable with the MOLA aeroid).

All the mapping was then finalized by using CTX (Context Camera onboard Mars Reconnaissance Orbiter, Malin et al., 2007) mosaic created using ISIS3 (Torson and Becker, 1997) with a spatial resolution of ~6 m/pixel. With the aid of such a high resolution dataset we were able to mark with a polygonal shapefile all the single vents in visible imagery, useful for further analyses.

Table 1
list of the datasets used for mapping and fractal clustering analysis.

Type of Dataset	Processing level	Spatial/grid Resolution (m/pixel)	Format
MOLA	MEGDR	460	GeoTiff, Shapefile
THEMIS	Daytime IR global mosaic	100	GeoTiff
THEMIS	Nighttime IR global mosaic	100	GeoTiff
HRSC	DA4	100	GeoTiff
HRSC	ND4	12.5	GeoTiff
CTX	level2	6.0	GeoTiff
Vents Mapping	N/D	N/D	shapefile, geodatabase
Global tectonics	N/D	N/D	shapefile, geodatabase

The mapped dataset consists of the vent locations, vent elongation (azimuth of the maximum axis of the ellipse inscribing the vent), length and strike of the faults. In this contribution, the small shields volcanoes in Syria Planum (Baptista et al., 2008) are named monogenetic vents because are dispersed and similar to the lava shield in Smith and Németh (2017).

The vent data set (292 vents) consists of the data in the supplementary material of Bleacher et al. (2009) and Richardson et al. (2013) plus the new vents mapped in this work. Since our objectives involve the analysis of vents population and their azimuthal distribution and elongation, we have reviewed the whole mapping present in literature by considering and contouring every single visible vent on CTX images rather than single volcanic center, and calculating their barycenter (see Supplementary materials for morphometric parameters and coordinates). We took into account only the vents falling within the

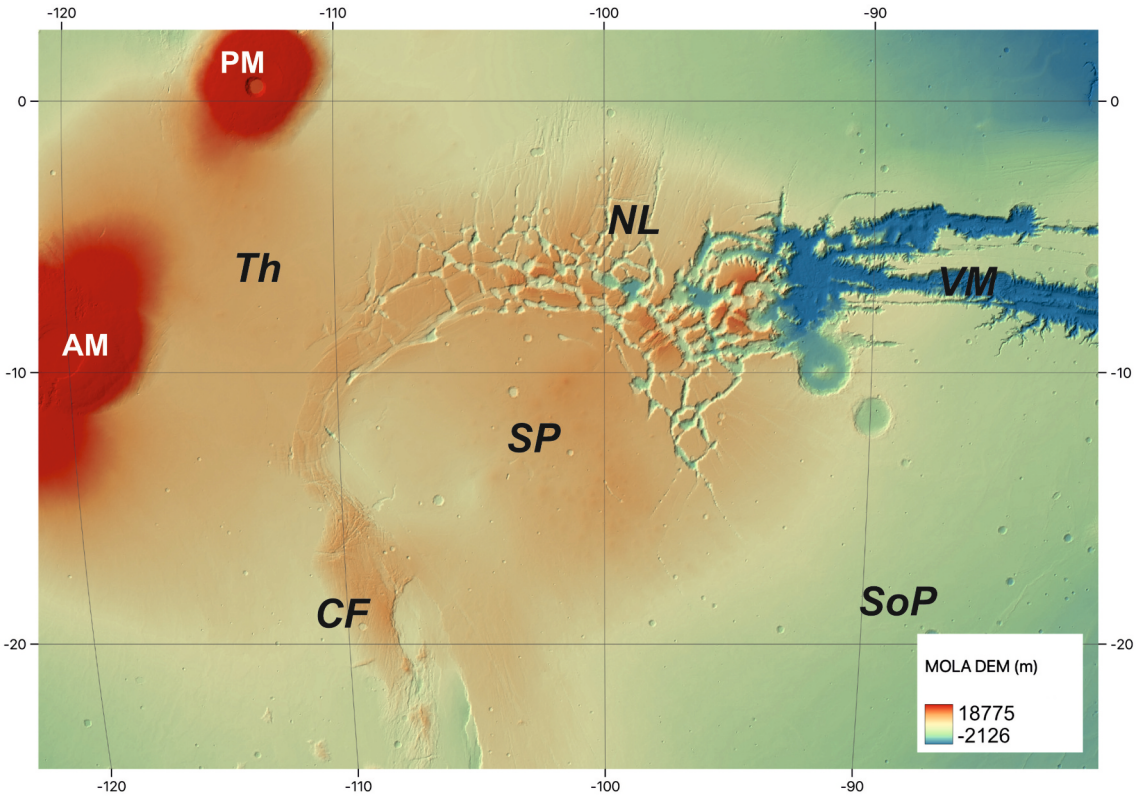

Fig. 1. Map of the main structures in the studied area. Th: Tharsis bulge; NL: Noctis Labirintus; SP: Syria Planum; CF: Claritas Fossae; VM: Valles Marineris; SoP: Solis Planum; AM: Ascreus Mons; PM: Pavonis Mons.

borders of the Syria Planum unit according to the geologic map of Tanaka et al. (2014) managing them in a GIS environment.

The main structures (faults, graben and fossae) have been mapped from Tanaka et al. (2014) and from Richardson et al. (2010) and (Richardson et al., 2021) (see Supplementary materials). The sinusoidal projection has been used with the reference meridian (260.5°E) placed in the barycenter of the convex hull of Syria Planum vents population as a whole. The sinusoidal projection allows minimizing deformation around the dataset in the proximity of the central longitude, which is a fundamental point in the reliability of the results, and results optimal since it is elongated and roughly oriented in NW-SE direction.

3. Methods

The extent of a volcanic field, defined by the spatial distribution of its vents, has been used previously to gain information on the volcanic feeding systems and on the tectonic setting at regional and local scales (Spörli and Eastwood, 1997; Tadini et al., 2014; Cañón-Tapia, 2021a, 2021b).

In the Syria Planum, vent clustering has been performed by using the nearest neighbour distance distribution (or vent separation, s). A multivariate analysis of the spatial distribution of the vents was performed using clustering approach based on an agglomerative hierarchical method and by analyzing the vent self-similar clustering (Mazzarini and Isola, 2010; Mazzarini and Isola, 2021; Pozzobon et al., 2015, 2021). The shape of the volcanic field was investigated by Principal Component Analysis (PCA) and Vent to Vent Distance (VVD) analysis as in Mazzarini et al. (2016).

3.1. Spatial clustering

3.1.1. Clustering analysis

Vents in volcanic fields typically cluster (Connor, 1990; Connor et al., 1992; Mazzarini, 2007; Le Corvec et al., 2013a). The determination of clusters is method sensitive and the use of different methods is recommended for a robust definition of the clusters (e.g., Cañón-Tapia, 2016, 2020). The vent's nearest neighbour distance (s) for each vent in the volcanic fields is investigated by applying the CV and R-c statistics and the agglomerative hierarchical method (see Appendix A1).

3.1.2. PCA and VVD analysis

The PCA and the VVD methods (see Appendix A2) proposed by Mazzarini et al. (2016) have been used for investigating the overall shape of the volcanic field. The shape of the volcanic field is then compared with the feeder azimuthal distribution derived from the mapping of vent elongations, vent alignments and coalescence and eruptive fissures (e.g., Le Corvec et al., 2013a; Isola et al., 2014; Mazzarini et al., 2016).

3.1.3. Self-similar clustering

In volcanic areas, the spatial distribution of monogenic vents (Mazzarini and Armienti, 2001; Mazzarini, 2007; Mazzarini and Isola, 2010) is linked to the fracture network that allows an efficient hydraulic connection between crustal/subcrustal fluid reservoirs and the surface (see Appendix A3). The actual geometric and physical properties of a percolating network are described by the percolation theory (Orbach, 1986; Stauffer and Aharony, 1994; Song et al., 2005). Percolation theory can thus be applied to the analysis of the fracture networks that allow fluids to move within the crust (i.e., Bonini and Mazzarini, 2010; Mazzarini and Isola, 2010; De Toffoli et al., 2018).

3.1.4. Two-dimensional symmetric Gaussian kernel

The spatial distribution of the vent density in the volcanic field (see Appendix A4) is computed by applying a two-dimensional, symmetric Gaussian kernel density estimate (e.g., Connor and Connor, 2009; Kiyosugi et al., 2012).

3.2. Structural analysis

A direct link between fractures and vents has been proposed for monogenetic constructs (cinder and spatter cones, domes, etc.) where their morphometric features (vent elongation, vent alignment) and their spatial distribution are closely related to fracture systems that feed them (e.g., Nakamura, 1977; Tibaldi, 1995; Takada, 1994; Le Corvec et al., 2013b; Muirhead et al., 2015).

The vents in Syria Planum were thus analyzed in terms of the azimuth distribution of the vent elongation weighted by the vent eccentricity; the eccentricity weight is computed for each vent as the ratio of its eccentricity to the minimum eccentricity value, the higher the vent eccentricity the higher the weight. Vent alignments were analyzed using the azimuth of the N(N-1)/2 lines connecting vents with lengths less or equal to a certain threshold (e.g., Richardson et al., 2021). According to Cebriá et al. (2011), the closer the vents the higher the probability that they are fed by the same fissure and, consequently, that they are aligned along a fracture. The threshold used in Cebriá et al. (2011) is $d \leq (\mu - \sigma)/3$, where μ is the average vent to vent distance and σ is the standard deviation. The structure of the volcanic field is compared to the azimuth distribution of the main fault systems in the neighbouring areas. The studied region where the Syria Planum volcanic field is located was gridded with cells 400 km in size; the azimuth distribution of fault segments in each cell was then displayed. At the scale of the volcanic field, a grid with cells 100 km in size was set up, and for each cell, the fracture intensity along with the azimuth distribution of the fractures was computed. Two trends are considered parallel or structurally similar within a $\pm$ 10° of azimuthal variation. The definition of the main structural trends is performed by visual inspection of the azimuth distribution and by the assements of a unimodal (von Mises) distribution of the trends (see Appendix B).

4. Geological Background

Syria Planum is located at 12°S 104°W (Nahm and Schultz, 2010), and it is bordered to the north and northwest by the Noctis Labyrinthus graben system, on the west by Claritas Fossae and on the SW and S sectors Solis Planum (Fig. 1).

On the eastern side, a large plain of ridged lava flows and tectonic structures are present (Nahm and Schultz, 2010). Covering a surface of 400 × 700 km^2 Syria Planum belongs to the upper member of the Syria Planum Formation (namely Hsu) according to the global geologic map of Mars by (Tanaka et al., 2014).

The vents have been divided into three main morpho-structural units by Baptista et al. (2008): (i) a group of 30 conical protuberances with 10–60 km diameter detected with MOLA, THEMIS and HRSC images identified as small volcanoes with slopes <3–10°, whose steepness is comparable to that of the large Tharsis Montes; (ii) widespread lobate-shaped lava flows erupted by the NW sector that can reach hundreds of km length, and (iii) highly fractured terrain on the Southern sector with large NE-SW trending grabens possibly related to the Tharsis Montes bulge.

Volcanic structures in Syria planum date back to 3 Ga (Richardson et al., 2021; Baptista et al., 2008; Hauber et al., 2011; Richardson et al., 2013), whereas the highest rate of magma emplacement activity is debated to be either Hesperian/early Amazonian or fully Amazonian with the activity peaking at ~1 Ga (Hauber et al., 2011). The Syria planum volcanic field have been dated with the crater counting technique (counting craters with diameters larger than 250 m, and using the Martian crater chronology function, Hartmann and Neukum, 2001) both by counting craters on single edifices, on the entire volcanic complex and on the lava flows extending to the South and South-East. Since the principle of crater counting, where an older surface retains a size frequency distribution of prevailing larger craters per area, only the cumulative Syria Planum extent was successfully dated, as the single volcanic edifices were too small to retain a sufficient amount of craters,

with also problems of obliterations by volcanic resurfacing, to date them correctly. The Syria Planum region as a whole resulted of Hesperian age (3.5–3.6 Ga) by (Baptista et al., 2008). Richardson et al. (2013) performed a more detailed analysis of the crater retention age using the 521 ppd THEMIS IR daytime global mosaic on craters larger than 500 m in accordance with vent groups and morphologic units and combining it with superposition relationships.

These ages show that the temporal span of formation of the whole Syria Planum volcanic construct is slightly longer than calculated previously by Baptista et al. (2008), most likely to be ascribed to the larger crater counting areas and higher resolution data available. Richardson et al. (2013) show that the main Syria construct started with Syria Mons central bulge in the Early Hesperian at 3.4–3.5 Ga whereas at 3.4–3.3 Ga a second shield formed at the center of Syria Planum and new extensional faulting developed. All the effusive activity continued spanning through the whole experian towards the Early Amazonian at 2.9–3.3 Ga with two groups of coalesced vents with the younger ones spreading towards the north (calculated with superposition of lava flows and single cones). This highlights at least three major volcanic episodes, with additional late-stage magmatism dated by Hauber et al. (2011) on some individual vents up to a few hundred million years.

Preliminary vent mapping has been performed by Baptista et al. (2008), resulting in 30 small volume shields cones. These small volume shields cones are similar to the small shields in Iceland (Rossi, 1996). Richardson et al. (2013) provided a more systematic study of the Syria Planum volcanic area mapping a significantly larger number of shields (263). The spatial relationship of the vents has been studied in terms of nearest neighbour and two-point azimuthal analysis (Richardson et al., 2013). The nearest neighbour analysis shows that all of the vents in Syria planum are clustered (Richardson et al., 2013) and this vent clustering has been interpreted as a record of different magma production episodes.

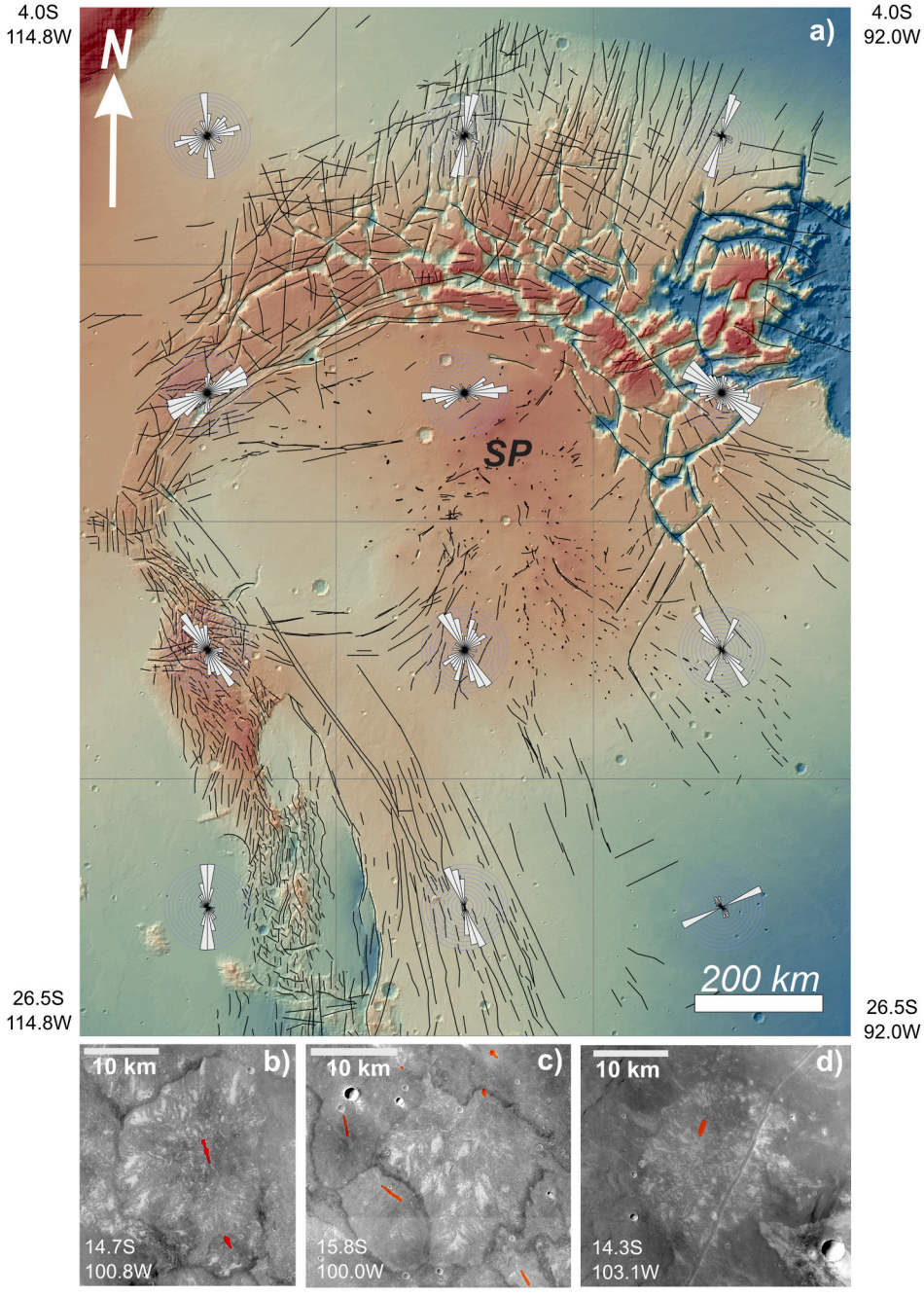

Fig. 2. a) map of the Syria Planum volcanic field (SP) and surroundings. The black solid lines are the main faults in the area derived from Tanaka et al. (2014) and from Richardson et al. (2013, 2021). The squared cells are 400 km wide; the rose diagrams represent the azimuth distributions of the fractures that fall within the cell (bin 20°). The lower panels show examples of Syria Planum volcanic cones with the vents mapped in red. It is clearly visible that most of the vents are strongly elliptical. In b) it is clearly visible the spreading of the flow from the central vent forming the volcanic edifice. In c) it is visible an arrangement of 3 different clustered edifices with fissure vents while in d) there is visible a fissure vent nearby a major NE-SW graben that crosscuts the volcanic cone itself. All these images are taken from CTX global mosaic at 6 m/pixel resolution. More examples are visible in Richardson et al., (Richardson et al., 2013; Richardson et al., 2021). (For interpretation of the references to colour in this figure legend, the reader is referred to the web version of this article.)

In Syria planum, fissure/vent shapes are roughly preferentially oriented towards the north-west, and with a possible radial orientation with respect to a hypothesized tectonic center between Noctis Labyrinthus and Pavonis Mons (Bleacher et al., 2009; Anderson et al., 2001 and references therein). The short inter-vent relationship was analyzed with a two-point azimuth method, in order to verify local correlations between eruptive centres and their neighbours (Bleacher et al., 2009).

In Syria Planum, volcanism evolved from a central vent volcano to dispersed shield field development over several hundred million years (Richardson et al., 2013) forming a NW-SE elongated volcanic field (the Syria Planum trend, SPT). During this period, independent magma bodies related to each small volcano interacted to some extent with one or more buried inherited fault systems, which are the NE-SW to ENE-WSW Tharsis Mons trend, the N-S to NNE-SSW Noctis Labyrintus trend, the NNW-SSE to N-S Claritas Fossae trend and the WNW-ESE to E-W Valles Marineris trend, respectively (Figs. 1 and 2).

5. Results

5.1. Fault systems

The analysis of the azimuth distribution of the main fractures (Figs. 2 and 3) indicates that the Syria Planum volcanic field developed as a whole nearly parallel to the NNW-SSE Claritas Fossae trend with portions with well-developed NE-SW Tharsis trend (Figs. 2, 3). In the north portion of the volcanic field, the NE-SW to ENE-WSW Tharsis Montes trend is well developed (Fig. 3).

In the Syria Planum area, the higher fracture intensity is located at its western and eastern borders, respectively (Fig. 3). In the west portion of the volcanic field, the highest fracture intensity values (44×10^{-3} and 33×10^{-3}) result from the occurrence of fault systems with TMT and NLT trends. In the east portion, the higher fracture intensity values (29×10^{-3} and 20×10^{-3}) are linked to faults with the NLT and SPT trends. At the scale of the volcanic field (Fig. 3), fracture systems with the NE-SW trend (TMT) are widespread in the northern and central part of the Syria Planum, while fracture systems with the NNW-SSW (CFT), the

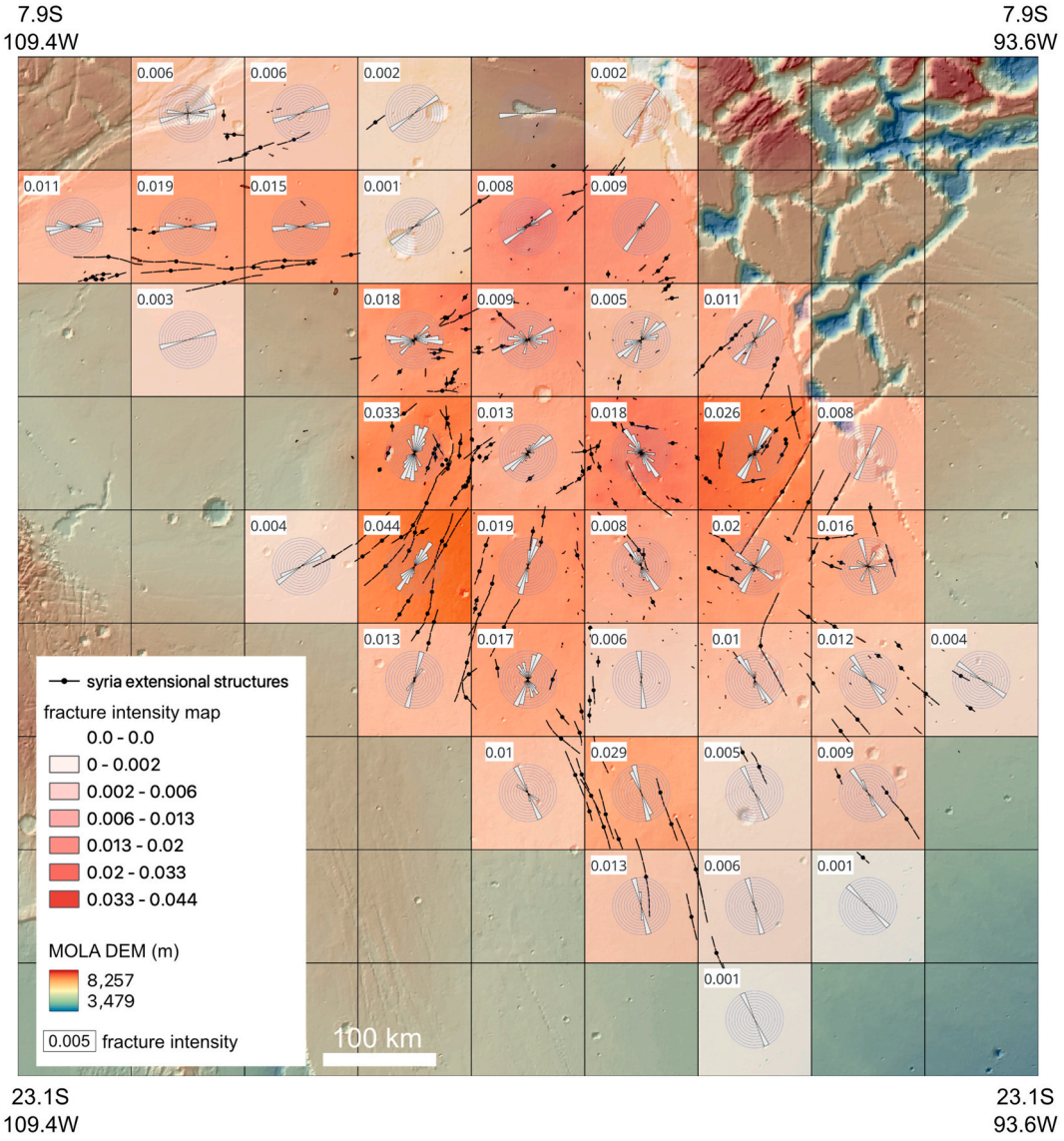

Fig. 3. Fracture intensity map in the Syria Planum. The fractures in the area are derived from Tanaka et al. (2014) and from Richardson et al. (2013, 2021) and integrated with our observations. The squared cells are 100 km wide, the rose diagrams represent the azimuth distributions of the fractures that are within the cell (bin 10°). The fracture intensity in each cell is represented by the colour of the cell and by the number in each cell. (For interpretation of the references to colour in this figure legend, the reader is referred to the web version of this article.)

NNE-SSW (NLT) and the NW-SE (SPT) trends are most developed in the south.

5.2. Vent clustering

Syria Planum has an average nearest neighbour distance (i.e., the vent separation, s) of 12.3 km showing a short- (CV > 1 in Table 2) and long- (R-c statistics in Table 2) range clustered distribution of the vents. The density distribution of the vents (Fig. 4) obtained by applying the two-dimensional, symmetric Gaussian kernel estimate (see Appendix A4, Eq. A4.1) clearly shows a clustering of the vents. The agglomerative hierarchical clustering (see appendix A1) detected four clusters (Table 2; Fig. 4). Cluster 1 shows only short-range clustering while cluster 2 has only a long-range clustering (Table 1). Cluster 3 is clustered at all scales while cluster 4 is not clustered at all scales (Table 2).

5.3. VVD and PCA analysis

Syria Planum volcanic field has a NW-SE (134°) elongated shape with an eccentricity of 0.4 as defined by the VVD and PCA analysis (Table 2; Fig. 5a). The VVD and PCA analysis have been performed also for the vent clusters that have eccentricity lower than that of the volcanic field (Table 2; Fig. 4).

Notably, none of the clusters has elongation parallel to that of the volcanic field; the southeastern most cluster (cluster 3, Table 2; Figs. 4 and 6) is elongated nearly parallel to the Syria Planum trend, whereas the other clusters have NE-SW elongations (Table 2; Figs. 4 and 6).

5.4. Volcanic field structures

The elongation of the vents and the vent alignments in the volcanic field have a polymodal azimuth distribution (Table 3) where the main peak trends NW-SE and the other minor peaks are almost parallel to the main structural trends in the area (Fig. 5b).

The degree of vent alignments has been analyzed by applying the method of Cebriá et al. (2011) to the lines connecting vents derived from the VVD analysis; this analysis shows an overall vent alignment in the NW-SE direction with a greater azimuth dispersion than the VVD analysis (Fig. 6a, first and second panels). The vent elongation weighted for the vent eccentricity (i.e., the higher the eccentricity the higher the weight) identifies the main NW-SE (SPT) trend which is more prominent than the NE-SW (TMT) trend (Fig. 6a, third and fourth panels). The PCA and VVD analyses have been performed also for the clusters (Fig. 6; Table 2).

The northernmost cluster (cluster 1) shows a NE-SW elongated shape (9° anticlockwise to the TMT trend) and a bimodal azimuth distribution of the vent alignments with a main WSW-ENE rotated 12° anticlockwise to the VMT trend and 22° clockwise to the TMT trend; a secondary WNW-ESE (21° clockwise to the VMT trend) peaks (Fig. 6b, first and second panels). The vent elongation shows a main WNW-ESE (13° clockwise to the VMT trend) peak (Fig. 6b, third and fourth panels).

Cluster 2 shows a dispersed VVD azimuth distribution with a NE-SW elongated shape (7° anticlockwise to the TMT trend) and a vent alignment characterized by a main NE-SW (8° anticlockwise to the TMT trend) peak and a secondary NW-SE (20° anticlockwise to the SPT trend) peak (Fig. 6c, first and second panels). The vent elongation has an azimuth distribution characterized by a well-defined main NE-SW (10° anticlockwise to the TMT trend) peak (Fig. 6c, third and fourth panels).

Cluster 3, the southernmost one, has an elongated shape and VVD azimuth distribution with a WNW-ESE (9° clockwise to the VMT trend) peak. Minor peaks trend N-S, 10° anticlockwise to NLT trend, and NNE-SSW, 10° clockwise to NLT trend (Fig. 6d, first panel). The vent alignment azimuth distribution shows a clear main NW-SE (SPT trend) and minor NW-SE (TMT trend) peaks (Fig. 6d, second panel). The vent elongation shows a clear main NW-SE (SPT trend) peak (Fig. 6d, third and fourth panels).

Cluster 4 has a dispersed azimuth distribution of the VVD lines with an overall NNE-SSW to NW-SE (19° anticlockwise to TMT trend) elongated shape (Fig. 6e, first panel). The vent alignment azimuth distribution is dispersed with a main well-defined N-S (10° anticlockwise to the NLT trend) peak and several minor peaks (Fig. 6e, second panel). The vent elongations have azimuth distributions very similar to that of the vent alignments (Fig. 6e, third panel) while the vent elongations weighted for the vent eccentricity (Fig. 6e, fourth panel) have a main NE-SW (TMT trend) peak, a secondary NNW-SSE (CFT trend) peak and a third N-S (NLT trend).

5.5. Volcanic field self-similar clustering

In Syria Planum, the self-similar clustering of vents (Eqs. A3.1 and A3.2 in Appendix A3) was investigated for the whole data set and for the identified clusters having at least 50 vents (Table 4).

For all the data sets, the self-similarity of the vents is well defined (see the *p* value in Table 4). The log-log plot of the whole field has a clear plateau with an upper cut off (Uco) of 110 km and a fractal exponent D of ~1.70 (Fig. 5c and 7a).

The 110 km upper cut off (Uco) is a common feature shared by the whole data set and by the three clusters (Table 4 and Fig. 7). Cluster 2 has a fractal exponent (D) ~1.69, cluster 3 has D ~ 1.39 and cluster 4 has D ~ 1.77 (Table 4 and Fig. 7).

6. Discussion

Considering the fractal exponent of the three relevant clusters of Syria Planum (see Table 4), cluster 3 (~1.4) shows the lower values. Cluster 2 in the NW sector shows a D value (~1.7), very similar to the D value of cluster 4 (~1.8). The vent self-similar clustering of the vents in Syria Planum suggests that the deep magma reservoir is about 100 km deep (Fig. 7; Table 4) indicating that a crust 100 km thick existed during the late stage dispersed volcanism. The inferred depth of the main magmatic reservoir is in accordance with the actual crustal thickness derived by MGS of ~90–110 km in correspondence with the Syria Planum bulge (Zuber et al., 2000; Neumann et al., 2004; Zuber, 2001).

In the Syria Planum volcanic field, the elongation of the volcanic field shape and the azimuth distribution of the vent elongations show a well expressed SPT (NW-SE) trend (Fig. 5a and b). The vent elongations (Fig. 5b) show secondary peaks parallel to the main structural trends of the area (Fig. 2 and Table 3). Notably, SPT trend is not clearly expressed

Table 2
Results of spatial clustering and PCA analysis for the Syria Planum volcanic field and its clusters.

Data	N	SM (m)	sm (m)	ŝ (m)	CV	R	c	p (<0.05)	az(°)	e
all	292	81,412	447	12,334	1.12	0.7157	−9.2926	1.5×10^{-20}	134°	0.40
cl1	29	76,971	865	17,440	1.20	0.9095	−0.9322	0.3513	46°	0.20
cl2	95	51,236	587	11,294	0.96	0.8673	−2.4744	0.0133	48°	0.24
cl3	70	81,412	447	13,851	1.35	0.8323	−2.6847	0.0073	98°	0.11
cl4	98	52,645	659	10,746	0.75	0.9983	−0.0328	0.9738	36°	0.18

N: number of vents; SM: maximum nearest neighbour distance; sm: minimum nearest neighbour distance; ŝ: average nearest neighbour distance; CV: coefficient of variation; R, c: values of R-c statistics; p: the probability that distribution is not clustered (H_0 hypothesis); az: azimuth of the maximum eigenvector from PCA; e: eccentricity from PCA.

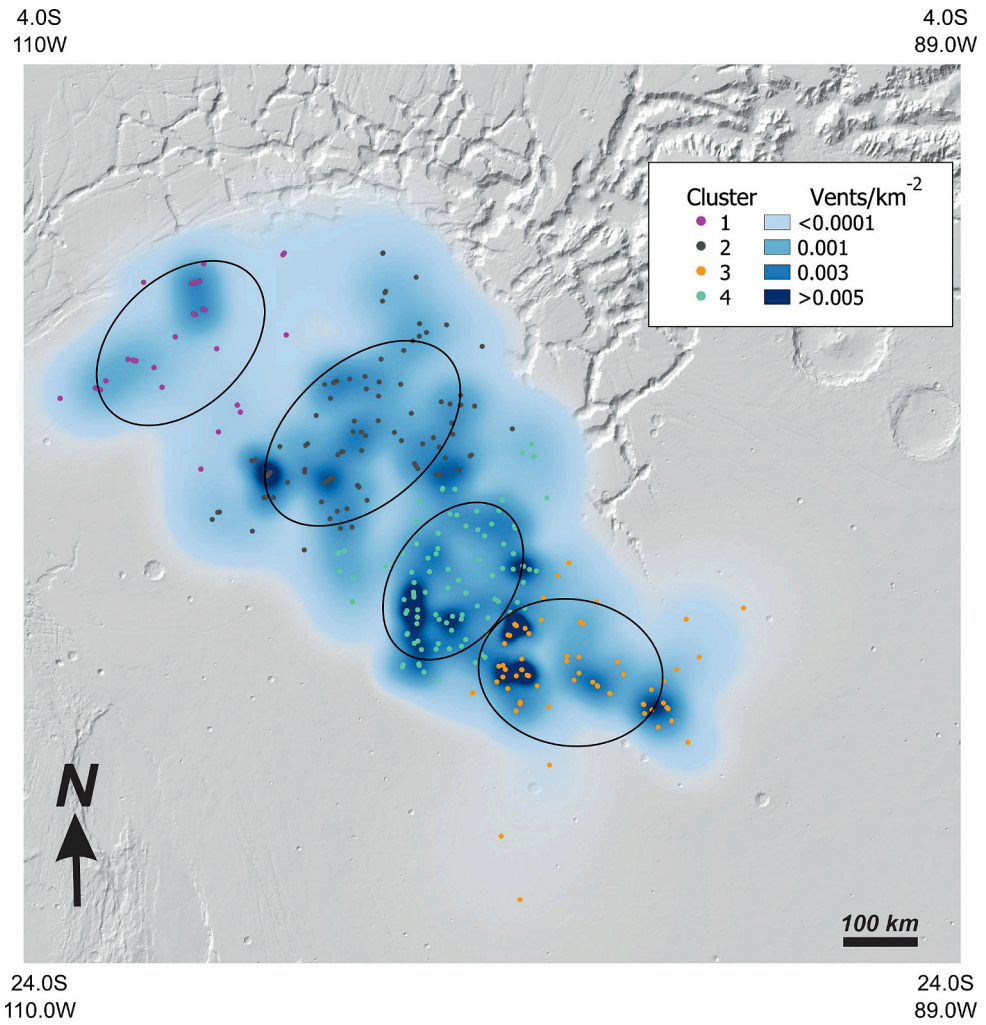

Fig. 4. Vent density distribution map by applying the Gaussian Kernel (see Appendix A4). The black ellipses are the PCA ellipses for each vent cluster in the Syria Planum volcanic field (Table 2).

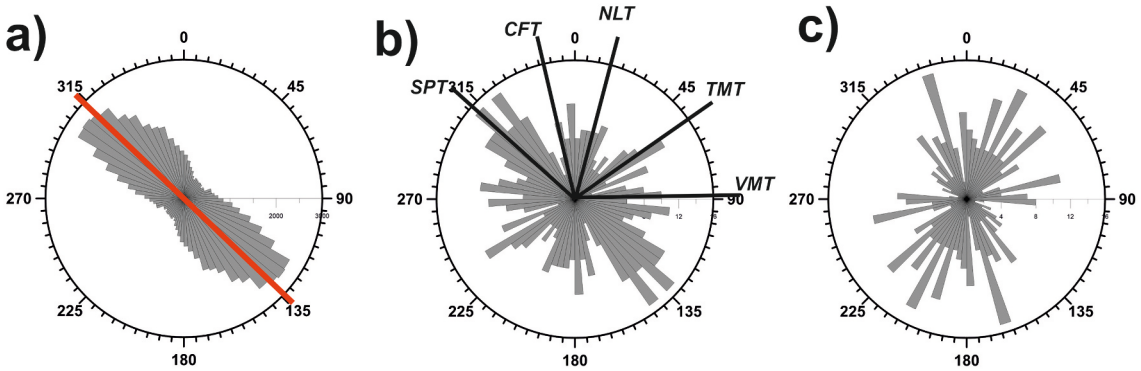

Fig. 5. a) Azimuth distribution of the vent-to-vent distances (VVD) and of the principal eigenvector of the PCA analysis (i.e. the main axis of the ellipse) of the Syria Planum volcanic field. b) Azimuth distribution of vent elongations, vent alignments and volcanic structures in the Syria Planum volcanic field (Table 3). SPT: Syria Planum trend; CFT: Claritas Fossae trend; NLT: Noctis Labyrinthus trend; TMT: Tharsis Montes trend; VMT: Valles Marineris trend. c) Azimuth distribution of extensional fractures (Fig. 4) in Syria Planum.

in the azimuth distribution of faults/fractures in the Syria Planum (Fig. 5c). Faults in the studied area show NNW-SSE (5° anticlockwise to CFT trend) and NE-SW (TMT trend) peaks. Secondary peaks trends nearly parallels (within 10°) to the NLT and VMT trends (Fig. 5c).

Three out of the four vent clusters identified in Syria Planum show elongated shapes at high angle to the elongation direction of the volcanic field (Figs. 4 and 6; Table 2). The cluster, in the northwest sector of the volcanic field, has the azimuth distribution of its structures (Fig. 6b) that does not match the nearly E-W trends of the faults (Fig. 3). Moving southeastward, in cluster 2 there is a partial match between the trend of faults in the area (Fig. 3) and the vent elongations (Fig. 6c). Cluster 4 shows an apparent coherence between the vent elongations

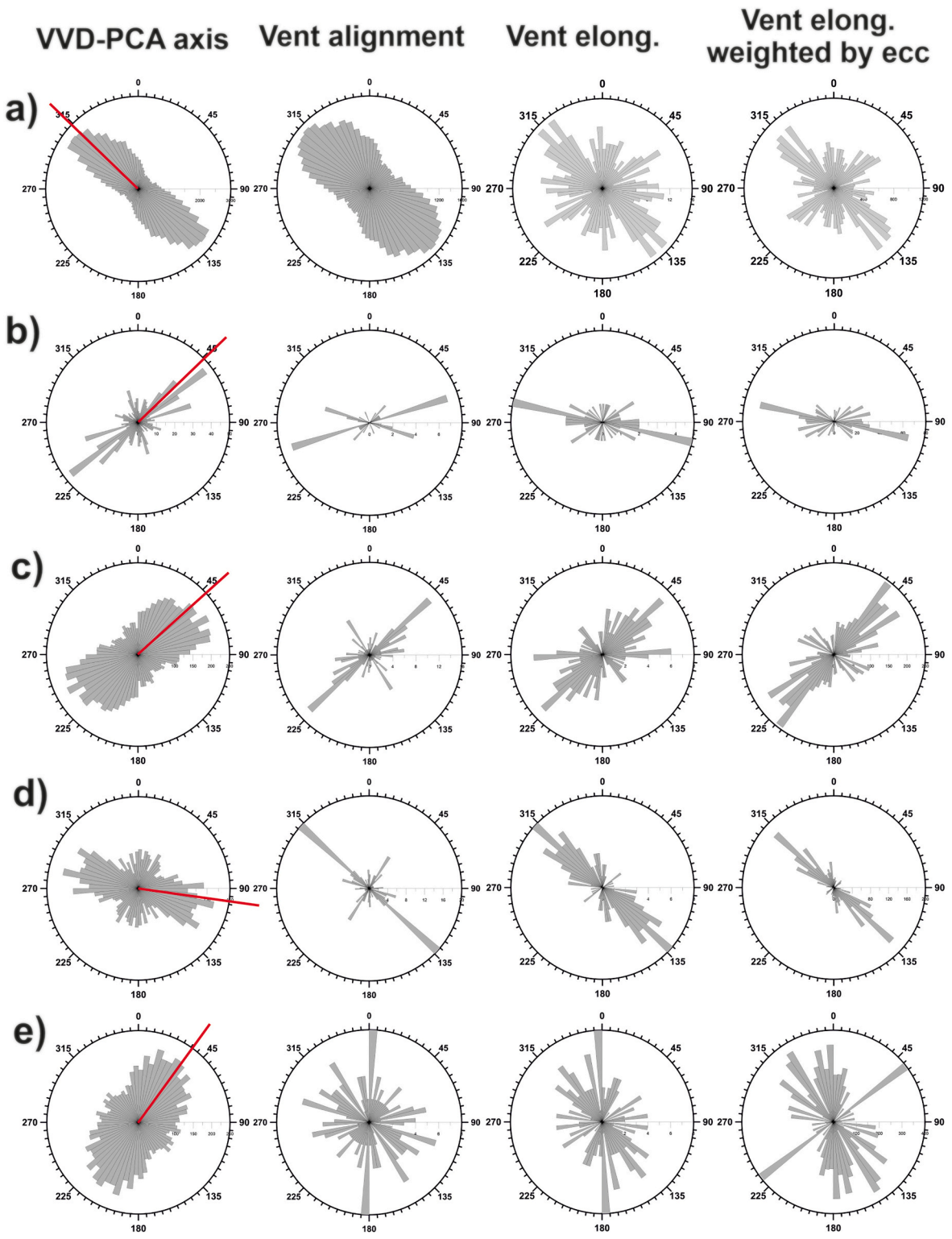

Fig. 6. In each row, from left to the right, the panels represent: the azimuth distribution of the vent-to-vent distances (VVD) and of the principal eigenvector of the PCA analysis (red line); the azimuth distribution of the vent alignment by applying the method of Cebriá et al. (2011); the azimuth distribution of the elongation of the vent; and the azimuth distribution of the vent elongation weighted by the vent eccentricity (the higher the eccentricity the more the weight). a) Syria Planum volcanic field; b) Cluster 1 (see Table 2); c) Cluster 2 (see Table 2); d) Cluster 3 (see Table 2); e) Cluster 4 (see Table 2). (For interpretation of the references to colour in this figure legend, the reader is referred to the web version of this article.)

(Fig. 6e) and the trend of faults (Fig. 3). The shape of the southeasternmost cluster 3 is 30° anticlockwise rotated to the NW-SE (SPT) trend; while the vent elongations show azimuth distribution with a clear NW-SE trending peak (Fig. 6 d) that matches the trend of the faults (Fig. 3).

The angular differences between the elongation of the whole volcanic field and its clusters and, in each cluster, between the vent elongation and the main fault trends may be interpreted as resulting from the evolutionary formation of the dispersed volcanism phase in Syria

Table 3
Circular statistics of the azimuth of the main structural trends in Syria Planum.

Trend	n	θ	95% conf int	R	P (<0.005)
SPT	87	132°	130°–135	0.9444	2.37×10^{-32}
CFT	36	167°	164°–170°	0.9603	6.12×10^{-14}
NLT	45	015°	013°–018°	0.9536	4.54×10^{-17}
TMT	50	055°	053°–057°	0.9561	5.09×10^{-19}
VMT	32	089°	085°–093°	0.9253	9.85×10^{-12}

n: number of elements; θ: circular mean (clockwise from North); conf int: confidence.
interval; R: Rayleigh's value; p: H_0 vs. von Mises distribution.

Table 4
Statistics of the self-similar clustering analysis for the Syria Planum volcanic field and for its clusters.

Data	N	b	D	R^2	p (uncorr)	Lco (km)	Uco (km)
all	292	4×10^{-10}	1.7023	0.9995	1.8×10^{-64}	13 ± 3	110 ± 10
cl2	95	1×10^{-9}	1.6896	0.9983	3.6×10^{-47}	18 ± 2	110 ± 10
cl3	70	5×10^{-8}	1.3869	0.9994	2.0×10^{-71}	9 ± 3	100 ± 10
cl4	98	5×10^{-10}	1.7887	0.9986	2.3×10^{-49}	16 ± 3	95 ± 10

N: number of vents; b: normalization coefficient; D: fractal exponent; R2: correlation coefficient; p: the probability that correlation does not exist; Lco: lower cut-off; Uco: upper cut-off.

Planum (Richardson et al., 2013).

According to Baptista et al. (2008) and Schultz (1998) the evolutionary sequence of the large-scale structural framework of Valles Marineris, Noctis Labyrinthus and Syria Planum volcanism consisted of a sequence of four macro-events: i) Late Noachian-Early Hesperian: formation of a graben system; ii) Late Hesperian (3.2 Ga) formation of Syria Planum main shield and effusion of fissure-fed flood basalts in NE-SW direction; iii) Early Amazonian (~1.8 Ga) crustal subsidence in the region of Syria Planum; iv) Late Amazonian formation of the main structures of Noctis Labyrinthus EW trending graben system and Noctis Labyrinthus structural framework. According to this reconstruction, the Syria Planum volcanic field is therefore part of a late-stage Amazonian volcanism, as it is set on and exploits an already well-developed structural framework, reflecting its main orientation according to each vent cluster location. In this case, the correlation between the inherited fabric and the volcanic lineament data suggests that magma exploited pre-existing lineaments and hence it is Late Amazonian.

Another possible explanation is that vent elongations and structures formed synchronously under the same stress regime. This scenario requires that the evolution of the dispersed volcanism in Syria Planum consisted of different volcanic phases each associated with the formation and the evolution of Tharsis Montes, Valles Marineris, Noctis Labyrinthus and Syria Planum structures. In this case, the dispersed volcanism in Syria Planum lasted for a long time span, from the late Hesperian to the early Amazonian.

Whatever the evolutionary history of the dispersed volcanism in Syria Planum, it shows a clear difference between the direction of the elongation of the volcanic field and its clusters with respect to the azimuth distribution of the structures (vent elongation, vent alignment, eruptive fissure) observed in the volcanic field (Fig. 3) suggesting that at a shallow crustal level, the magma exploited the actual fracture network that is not necessarily linked to the geometry of the whole volcanic field. The influence of the fracture network at shallow crustal levels on the propagation of dikes and on the site of eruption in volcanic fields has been shown by analogue models (Le Corvec et al., 2013b).

On Earth, several examples document how the structural grain of the shallow crust ultimately controls the eruption site of vents and their spatial distribution. The Pleistocene Auckland volcanic field is a clear example of volcanic field whose overall shape is controlled by deep lithospheric structures (e.g., Spörli and Eastwood, 1997). Nonetheless, in the Auckland volcanic field, the actual spatial distribution of vents as well as their morphology are controlled by the shallow crust fault/fracture network (Cassidy and Locke, 2010; Kereszturi et al., 2014).

In the off-shore of New Zealand, southern island, the analysis of borehole-constrained 2D seismic reflection data shows that upper crustal structures controlled the location of vents also for the fossil (Cretaceous-Eocene) Tuatara volcanic fields (Phillips and Magee, 2020).

In the East African Rift, the shape and elongation of volcanic fields are clearly linked to lithospheric-scale structures whereas the internal spatial distribution of vents is controlled by the shallow fracture network (Mazzarini and Isola, 2022).

The vent spatial distribution in volcanic field also gathers information on the geometries of the plumbing system at different depths as for the Jeju Island, South Korea volcanic field (Cañón-Tapia, 2021b). Parallelism between the shape of volcanic fields, the cone elongation and alignment to the maximum crustal horizontal stress has been observed in areas of active tectonic such as the Yucca Mountain (Connor et al., 2000) and the northern Main Ethiopian Rift (e.g., Rooney et al., 2011; Mazzarini et al., 2016).

In summary, the plumbing system of the Syria Planum consists of a deep portion at about 100 km. There is a clear dichotomy between the overall shape of the volcanic field and the direction of the feeders associated with the vents indicating that the deep portion of the plumbing system likely controlled the site and the overall shape of the volcanic field, whereas the shallow plumbing system is ruled by inherited structures that controlled the cone elongation, alignment and distribution.

Volcanic field plumbing systems consisting of a deep and a shallow portion have been reported also on Earth in the East African Rift System, for several volcanic fields where the location of the deep magma reservoir is controlled by lithospheric scale structures/geometries and the vent surface distribution and structures are controlled by inherited, shallow crustal, structures (Mazzarini and Isola, 2021, 2022; Le Gall et al., 2008).

7. Conclusions

In this work, we have carried out a thorough analysis of the volcanic field in Syria Planum region of Mars, and studied its relation with the major tectonic framework and the time evolution of the region. Four main clusters can be identified among the volcanic vents population and their spatial distribution has been analyzed in terms of fractal clustering. The fractal nature of the plumbing system enabled us to infer the depth of the source magmatic reservoir being located at ~100 km of depth. The eruptive structures, their distribution and the elongation of their vents indeed reflect a well-known process on Earth where large and diffused volcanic fields develop in correspondence of a deep magmatic reservoir and depend on its size, whereas their surface distribution is highly controlled by shallow crustal inherited structures. This makes the Syria Colles in Syria Planum a late-stage magmatic event which could have developed after the formation of the main regional structural framework of Claritas Fossae, Tharsis Montes, Noctis Labyrinthus and Valles Marineris or, alternatively, that formed through different volcanic phases coeval with the formation of the main structure in the region.

Declaration of Competing Interest

None.

Data availability

Data will be made available on request.

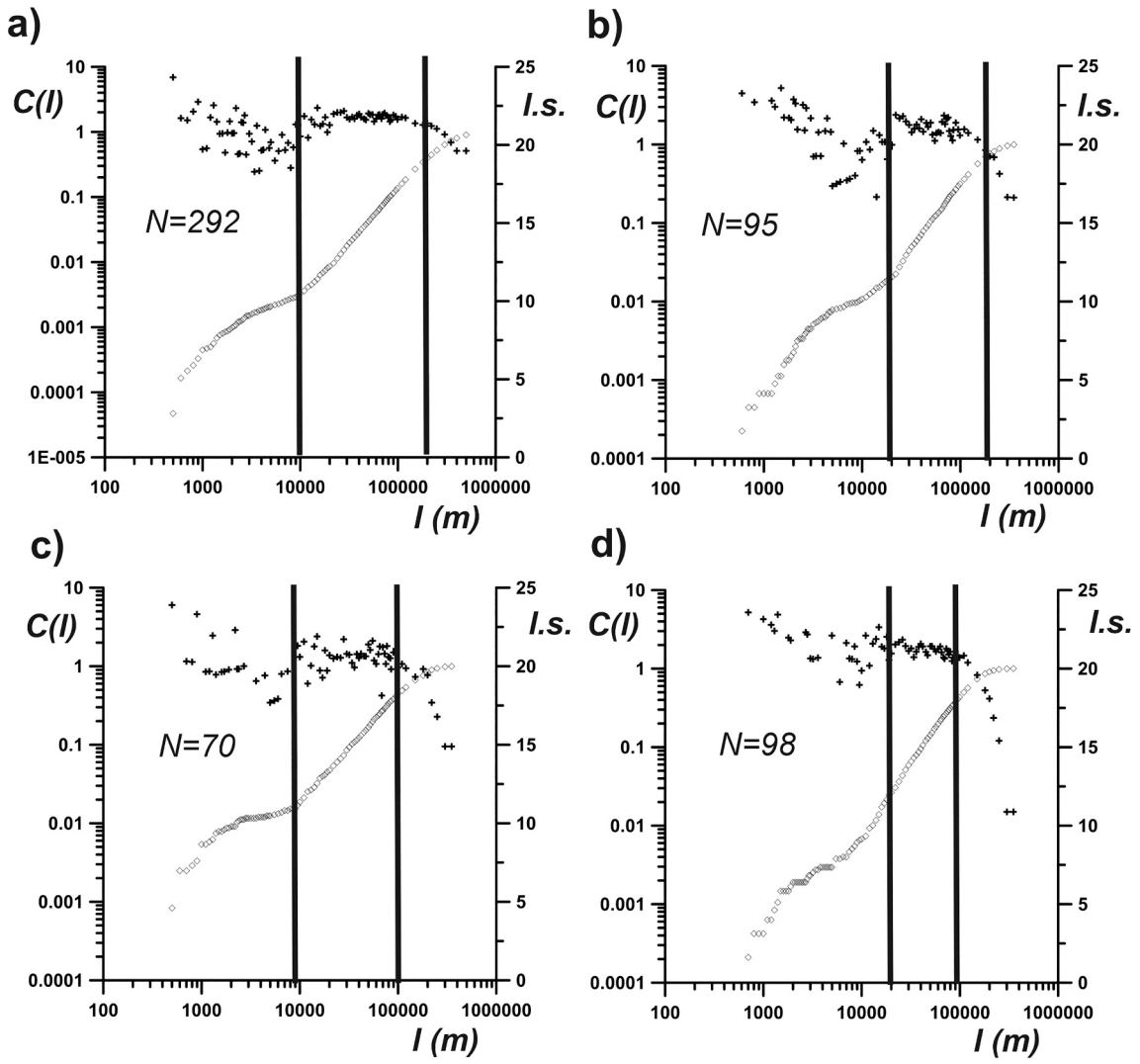

Fig. 7. Log-log plot of the vent self-similar clustering (see appendix A3), N is the number of vents in each data set. The size range is defined by the thick black vertical lines (see Fig. 4c). a) Syria Planum (Table 4); b) Cluster 2 (Table 4); c) Cluster 3 (Table 4); d) Cluster 4 (Table 4).

Appendix A. Methods used in the spatial distribution analysis of vents and fractures

A.1. Hierarchical Clustering and nearest neighbour distance analysis

Two statistical methods have been used for analyzing the nearest neighbour distance (s) of vents. The ratio between the standard deviation and the mean of the sampled population is the coefficient of variation (CV; Gillespie et al., 1999); CV > 1 indicates the clustering of points, CV = 1 is for a random or Poisson distribution, and CV < 1 is for anti-clustering (a homogeneous distribution). The CV statistic investigates how close points are to each other giving information on short-range clustering not probing the pattern of point distribution.

The R-c statistics (Clark and Evans, 1954) compare the actual nearest neighbour distance distribution with that expected for a Poisson distribution of N points. The reference density is the ratio between the actual point number (N) and the area of the convex hull containing them. $R < 1$ is for clustering and for a statistically significant departure from randomness at 0.95 and 0.99 confidence levels, $|c|$ should be >1.96 and 2.58, respectively. In particular, in the case of not very large points number, the scavenged statistic has been used (e.g., Baloga et al., 2007; Beggan and Hamilton, 2010).

The definition of the number of statistically significant clusters has been performed by applying a clustering analysis based on an agglomerative hierarchical method (e.g., Mazzarini, 2007; Mazzarini and Isola, 2010). The optimal number of clusters is derived from the analysis of the dendrogram that depicts the amalgamation of observations into one cluster. The similarity at any step is the per cent of the maximum distance at that step relative to the initial maximum inter-observation distance (i.e., the maximum distance between the points). An abrupt change in the similarity marks the point for cutting the dendrogram defining the number of clusters statistically significant in the data sets.

A.2. PCA and VVD analysis

The PCA analysis provides the shape (ellipse) of the volcanic field and the direction of the first eigenvector represents the trend of the long axis of the ellipse and can be used as a proxy for the field elongation (Mazzarini et al., 2016). The VVD method analyses the azimuth distribution of each of the

N(N−1)/2 segments connecting vent pairs. Well-aligned vents will produce a narrow well-defined peak in the azimuth distribution of segments connecting vents and small angular dispersion (i.e. well defined unimodal azimuth distribution). The dispersed distribution of vents or patterned distribution - en echelon vent alignments and vent clusters - will produce several peaks in the azimuth distribution of segments connecting vents (Mazzarini et al., 2016). These analyses have been performed also for selected clusters of volcanic fields derived from the hierarchical clustering.

A.3. Self-similar clustering

The self-similar clustering of vents has been investigated by applying the two-point correlation function method. For a population of N points (i.e. vents), the correlation integral is defined as the correlation sum (C(l)) that accounts for all the points at a distance of less than a given length l (Bonnet et al., 2001 and references therein). The term is computed as.

$$C\ (l) = 2\ N\ (l)/(N\ (N-1)\ ) \tag{A3.1}$$

where N(l) is the number of pairs of points whose distance is less than l.

The fractal distribution is defined by.

$$C\ (l) = bl^{D} \tag{A3.2}$$

with b being the normalization constant and D the fractal exponent.

The slope of the curve in a log(C(l)) versus log(l) diagram yields the D value.

The computed D value (fractal exponent of clustering) holds for a defined range of distances (size range) where the equation is valid. For each analysis, the size range of samples is in turn defined by a plateau in Δlog(C(l))/Δlog(l) (i.e., the local slope) versus log(l) diagram. The wider the range the better the computation of the power-law distribution (Walsh and Watterson, 1993). The choice of the zones where the plateau is well-defined and the determination of the lower and upper cutoffs (Lco and Uco, respectively) are done by selecting the wider length range for which the correlation between log(l) and the local slope is greatest (Mazzarini, 2004). A size range of at least one order of magnitude and at least 50 samples is required to extract robust parameter estimates (Bonnet et al., 2001; Andre-Mayer and Sausse, 2007; Clauset et al., 2009). The random removal of 20% of the analyzed samples from large datasets (i.e., > 200 vents) does not affect the estimation of fractal dimension (<0.01% of variation) and the error introduced into the estimation of the cut-offs is <1%–2% (Mazzarini and Isola, 2010). Mazzarini et al. (2013) tested the effect of uncertainties in point-like feature locations by adding random errors to the sampled points (in the 0–100 m, 0–300 m and 0–500 m ranges, i.e., errors as high as 5 to 25 times that of the coarsest image resolution used to locate the points). The 0–100 m errors randomly added to the point (vent) locations generated fractal exponent and cut-off values identical to those computed for the original dataset. In the case of 0–500 m random errors, the resulting fractal exponent was 3% higher than that computed for the original dataset, and the cut-offs' were very similar to those computed for the original dataset (Mazzarini et al., 2013).

The upper cut off value (Uco) obtained by analyzing several volcanic fields on Earth linearly scales with the depth of the fluid source (e.g., Mazzarini and Isola, 2010). This relationship has been observed for volcanic vents located in different geotectonic settings such as in the East African Rift (Mazzarini, 2007; Mazzarini and Isola, 2010), southern Patagonia (Mazzarini and D'Orazio, 2003; Mazzarini et al., 2008), TransMexican Volcanic Belt in Mexico (Mazzarini et al., 2010) and for mud volcanoes in the Greater Caucasus in Azerbaijan (Bonini and Mazzarini, 2010).

A.4. Two-dimensional symmetric Gaussian kernel

The two-dimensional, symmetric Gaussian kernel density estimate (e.g., Connor and Connor, 2009; Kiyosugi et al., 2012; Connor et al., 2019) is computed as follows:

$$\lambda(x) = \frac{1}{2N\pi h_i^2}\sum_i^N e^{-\frac{d_i^2}{2h_i^2}} \tag{A4.1}$$

d_i is the distance between location x and the N vents, and h_i is the smoothing bandwidth for vent i. Distance values between neighbour samples larger than h_i have a small weight in the computation of the density estimate. A variable bandwidth value has been applied by computing the half value of the distance between each sample and its nearest sixth neighbour (Favalli et al., 2012). The vent density maps of the volcanic field have been created by applying Eq. (A4.1); the resulting matrix possesses cells with the appropriate vent density value (vent/km^2).

Appendix B. Circular statistics

The definition of the azimuth of the axial data (i.e., cone elongation, fissure trend, vent alignment) has been assessed by use of the circular statistics (i.e. Mardia, 1972; Davis, 2002) and the PAST 4.12 statistical software (https://www.nhm.uio.no/english/research/resources/past/).

As first step, all data are plotted together for a visual inspection of possible trends and polymodal distributions. A buffer of about 10° is used for the azimuth of each main peak for sampling the data. On the sampled data the, circular mean is computed (Eq. B1); the 95% confidence interval on the mean is estimated according to Fisher (1983).

$$\overline{\theta} = tan^{-1}\frac{\sum sin\theta_i}{\sum cos\theta_i} \tag{B1}$$

The von Mises distribution is estimated by the computation of Rayleigh's parameter (R; Eq. B2)

$$R = tan^{-1}\frac{\sqrt{\left(\sum_1^n cos\theta_i\right)^2 + \left(\sum_1^n sin\theta_1\right)^2}}{n^2} \tag{B2}$$

and by the estimation of the probability of rejection of the null hypothesis (H0) at the 0.005 level of confidence (p).

Appendix C. Supplementary data

Supplementary data to this article can be found online at https://doi.org/10.1016/j.jvolgeores.2023.107830.

References

Anderson, R.C., Dohm, J.M., Golembek, M.P., Haldemann, A.F.C., Franklin, B.J., Tanaka, K.L., Lias, J., Peer, B., 2001. Primary centers and secondary concentrations of tectonic activity through time in the western hemisphere of Mars. J. Geophys. Res. 106, 20563–20585. https://doi.org/10.1029/2000JE001278.

Anderson, R.C., Dohm, J.M., Haldemann, A.F.C., Hare, T.M., Baker, V.R., 2004. Tectonic histories between Alba Patera and Syria Planum, Mars. Icarus 171, 31–38.

Andre-Mayer, A.-S., Sausse, J., 2007. Thickness and spatial distribution of veins in a porphyry copper deposit, Rosia Poieni, Romania. J. Struct. Geol. 29, 1695–1708. https://doi.org/10.1016/j.jsg.2007.06.010.

Baloga, S.M., Glaze, L.S., Bruno, B.C., 2007. Nearest neighbor analysis of small features on Mars: applications to tumuli and rootless cones. J. Geophys. Res. 112, E03002. https://doi.org/10.1029/2005JE002652.

Baptista, A.R., Mangold, N., Ansan, V., Baratoux, D., Lognonné, P., Alves, E.I., Williams, D.A., Bleacher, J.E., Masson, P., Neukum, G., 2008. A swarm of small shield volcanoes on Syria planum, mars. J. Geophys. Res. 113, 1–19. https://doi.org/10.1029/2007JE002945.

Beggan, C., Hamilton, C.W., 2010. New image processing software for analyzing object size-frequency distributions, geometry, orientation, and spatial distribution. Comput. Geosci. 36, 539–549. https://doi.org/10.1016/j.cageo.2009.09.003.

Bistacchi, N., Massironi, M., Baggio, P., 2004. Large-scale fault kinematic analysis in Noctis Labyrinthus (Mars). Planetary and Space Science 52 (1–3), 215–222. https://doi.org/10.1016/j.pss.2003.08.015.

Bleacher, J.E., Glaze, L.S., Greeley, R., Hauber, E., Baloga, S.M., Sakimoto, S.E.H., Williams, D.A., Glotch, T.D., 2009. Spatial and alignment analyses for a field of small volcanic vents south of Pavonis Mons and implications for the Tharsis province, Mars. J. Volcanol. Geotherm. Res. 185, 96–102. https://doi.org/10.1016/j.jvolgeores.2009.04.008.

Bonini, M., Mazzarini, F., 2010. Mud volcanoes as potential indicators of regional stress and pressurized layer depth. Tectonophysics 494, 32–47.

Bonnet, E., Bour, O., Odling, N.E., Davy, P., Main, I., Cowie, P., Berkowitz, B., 2001. Scaling of fracture systems in geological media. Rev. Geophys. 39 (2001), 347–383. https://doi.org/10.1029/1999RG000074.

Brož, P., Hauber, E., 2012. A unique volcanic field in Tharsis, Mars: Pyroclastic cones as evidence for explosive eruptions. Icarus 218, 88–99. https://doi.org/10.1016/j.icarus.2011.11.030.

Brož, P., Hauber, E., Wray, J.J., Michael, G., 2017. Amazonian volcanism inside Valles Marineris on Mars. Earth Planet. Sci. Lett. 473, 122–130. https://doi.org/10.1016/j.epsl.2017.06.003.

Brustel, C., Flahaut, J., Hauber, E., Fueten, F., Quantin, C., Stesky, R., Davies, G.R., 2017. Valles Marineris tectonic and volcanic history inferred from dikes in eastern Coprates Chasma. J. Geophys. Res. Planets 122, 1353–1371. https://doi.org/10.1002/2016JE005231.

Cañón-Tapia, E., 2016. Reappraisal of the significance of volcanic fields. J. Volcanol. Geotherm. Res. 310, 26–38.

Cañón-Tapia, E., 2020. Influence of method selection on clustering analyses of point-like features: examples from three zones of distributed volcanism. Geomorphology 354, 107063. https://doi.org/10.1016/j.geomorph.2020.107063.

Cañón-Tapia, E., 2021a. Volcano distribution and tectonics: a planetoidic perspective. In: Foulger, G.R., Hamilton, L.C., Jurdy, D.M., Stein, C.A., Howard, K.A., Stein, S. (Eds.), In the Footsteps of Warren B. Hamilton: New Ideas in Earth Science: Geological Society of America Special Paper, 553, pp. 1–11. https://doi.org/10.1130/2021.2553(08).

Cañón-Tapia, E., 2021b. Vent distribution on Jeju Island, South Korea: Glimpses into the subvolcanic system. Journal of Geophysical Research, Solid Earth 126. https://doi.org/10.1029/2021JB022269 e2021JB022269.

Cassidy, J., Locke, C.A., 2010. The Auckland volcanic field, New Zealand: Geophysical evidence for structural and spatio-temporal relationships. Journal of Volcanology and Geothermal Research 195, 127–137.

Cebriá, J.M., Martín-Escorza, C., López-Ruiz, J., Morán-Zenteno, D.J., Martiny, B.M., 2011. Numerical recognition of alignments in monogenetic volcanic areas: examples from the Michoacán-Guanajuato Volcanic Field in Mexico and Calatrava in Spain. J. Volcanol. Geotherm. Res. 201, 73–82.

Clark, P.J., Evans, F.C., 1954. Distance to nearest neighbor as a measure of spatial relationships in populations. Ecology 35 (4), 445–453.

Clauset, A., Shalizi, C.R., Newman, M.E.J., 2009. Power-law distributions in empirical data. SIAM Rev. 51, 661–703. https://doi.org/10.1137/070710111.

Connor, C.B., 1990. Cinder cone clustering in the trans mexican volcanic belt: implications for structural and petrologic models. Journal of Geophysical Research 95, 19,395–19,405. https://doi.org/10.1029/JB095iB12p19395.

Connor, C.B., Connor, L.J., 2009. Estimating spatial density with kernel methods. In: Connor, C.B., Chapman, N.A., Connor, L.J. (Eds.), Volcanic and Tectonic Hazard Assessment for Nuclear Facilities. Cambridge University Press, pp. 346–368.

Connor, C.B., Condit, C.D., Crumpler, L.S., Aubele, J.C., 1992. Evidence of regional structural controls on vent distribution: Springerville Volcanic Field, Arizona. Journal of Geophysical Research 97, 12,349–12,359. https://doi.org/10.1029/92JB00929.

Connor, C.B., Stamatakos, J.A., Ferrill, D.A., Hill, B.E., Ofoegbu, G.I., Conway, F.M., Sagar, B., Trapp, J., 2000. Geologic factors controlling patterns of small-volume basaltic volcanism: Application to a volcanic hazards assessment at Yucca Mountain, Nevada. Journal of Geophysical Research 105 (1), 417–432.

Connor, C.B., Connor, L.J., Germa, A., Richardson, J.A., Bebbington, M., Gallant, E., Saballos, J.A., 2019. How to use kernel density estimation as a diagnostic and forecasting tool for distributed volcanic vents. Statistics in Volcanology 4 (3), 1–25. https://doi.org/10.5038/2163-338X.4.3.

Davis, J.C., 2002. Statistics and Data Analysis in Geology, 3rd edition. Wiley, p. 656.

De Toffoli, B., Pozzobon, R., Mazzarini, F., Orgel, C., Massironi, M., Giacomini, L., Mangold, N., Cremonese, G., 2018. Estimate of depths of source fluids related to mound fields on Mars. Planetary and Space Science 164, 164–173. https://doi.org/10.1016/j.pss.2018.07.005.

Edwards, C.S., Nowicki, K.J., Christensen, P.R., Hill, J., Gorelick, N., Murray, K., 2011. Mosaicking of global planetary image datasets: 1. Techniques and data processing for thermal Emission Imaging System (THEMIS) multi-spectral data. J. Geophys. Res. 116, E10008. https://doi.org/10.1029/2010JE003755.

Favalli, M., Tarquini, S., Papale, P., Fornaciai, A., Boschi, E., 2012. Lava flow hazard and risk at Mt. Cameroon volcano. Bulletin of Volcanology 74 (2), 423–439.

Fisher, N.I., 1983. Comment on "a Method for estimating the Standard Deviation of Wind Directions". J. Appl. Meteorol. Climatol. 22 (11), 1971. https://doi.org/10.1175/1520-0450(1983)022<1971:COMFET>2.0.CO;2.

Gillespie, P.A., Johnston, J.D., Loriga, M.A., McCaffrey, K.J.W., Walsh, J.J., Watterson, J., 1999. Influence of layering on vein systematics in line samples. In: McCaffrey, K.J.W., Lonergan, L., Wilkinson, J.J. (Eds.), Fractures, Fluid Flow and Mineralization. Geol. Soc 155. Spec. Publ, London, pp. 35–56.

Greeley, R., 1977. Basaltic "plains" volcanism. In: Greeley, R., King, J.S. (Eds.), Volcanism of the Eastern Snake River Plain, Idaho: A Comparative Planetary Geology Guidebook, NASA CR-154621. NASA, Washington, DC, pp. 23–44.

Hartmann, W.K., Neukum, G., 2001. Cratering chronology and the evolution of Mars. Space Sci. Rev. 96 (1–4), 165–194.

Hauber, E., Bleacher, J., Gwinner, K., Williams, D., Greeley, R., 2009. The topography and morphology of low shields and associated landforms of plains volcanism in the Tharsis region of Mars. J. Volcanol. Geotherm. Res. 185, 69–95. https://doi.org/10.1016/j.jvolgeores.2009.04.015.

Hauber, E., Brož, P., Jagert, F., Jodłowski, P., Platz, T., 2011. Very recent and wide-spread basaltic volcanism on Mars. Geophys. Res. Lett. 38, L10201. https://doi.org/10.1029/2011GL047310.

Hiesinger, H., Head, J.W., Neukum, G., 2007. Young lava flows on the eastern flank of Ascraeus Mons: Rheological properties derived from High Resolution Stereo Camera (HRSC) images and Mars Orbiter Laser Altimeter (MOLA) data. J. Geophys. Res. 112, E05011. https://doi.org/10.1029/2006JE002717.

Isola, I., Mazzarini, F., Bonini, M., Corti, G., 2014. Spatial variability of volcanic features in early-stage rift settings: the case of the Tanzania Divergence, East African rift system. Terra Nova 26, 461–468.

Jaumann, R., Neukum, G., Behnke, T., Duxbury, T.C., Eichentopf, K., Flohrer, J., Gasselt, S., Giese, B., Gwinner, K., Hauber, E., 2007. The high-resolution stereo camera (HRSC) experiment on Mars Express: Instrument aspects and experiment conduct from interplanetary cruise through the nominal mission. Planet. Space Sci. 55, 928–952. https://doi.org/10.1016/j.pss.2006.12.003.

Kereszturi, G., Németh, K., Cronin, S.J., Procter, J., Agustín-Flores, J., 2014. Influences on the variability of eruption sequences and style transitions in the Auckland Volcanic Field. New Zealand Journal of Volcanology and Geothermal Research 286, 101–115.

Kiyosugi, K., Connor, C.B., Wetmore, P.H., Ferwerda, B.P., Germa, A.M., Connor, L.J., Hintz, A.R., 2012. Relationship between dike and volcanic conduit distribution in a highly eroded monogenetic volcanic field: San Rafael, Utah, USA. Geology 40 (8), 695–698.

Kling, C.L., Byrne, P.K., Atkins, R.M., Wegmann, K.W., 2021. Tectonic deformation and volatile loss in the formation of Noctis Labyrinthus, Mars. Journal of Geophysical Research, Planets 126. https://doi.org/10.1029/2020JE006555 e2020JE006555.

Le Corvec, N., Spörli, K.B., Rowland, J., Lindsay, J., 2013a. Spatial distribution and alignments of volcanic centers: clues to the formation of monogenetic volcanic fields. Earth-Science Reviews 124, 96–114. https://doi.org/10.1016/j.earscirev.2013.05.005.

Le Corvec, N., Menand, T., Lindsay, J., 2013b. Interaction of ascending magma with pre-existing crustal fractures in monogenetic basaltic volcanism: an experimental approach. Journal of Geophysical, Research, Solid Earth 118, 968–984. https://doi.org/10.1002/jgrb.50142.

Le Gall, B., Nonnotte, P., Rolet, J., Benoit, M., Guillou, H., Mousseau-Nonnotte, M., Albaric, J., Deverchere, J., 2008. Rift propagation at craton margin. Distribution of faulting and volcanism in the North Tanzanian Divergence (East Africa) during Neogene times. Tectonophysics 448, 1–19.

Malin, M.C., Bell, J.F., Cantor, B.A., Caplinger, M.A., Calvin, W.M., Clancy, R.T., Edgett, K.S., Edwards, L., Haberle, R.M., James, P.B., Lee, S.W., Ravine, M.A., Thomas, P.C., Wolff, M.J., 2007. Context Camera Investigation on board the Mars

Reconnaissance Orbiter. J. Geophys. Res. E Planets 112, 1–25. https://doi.org/10.1029/2006JE002808.
Mardia, K.V., 1972. Statistics of Directional Data. Academic Press, p. 380.
Mazzarini, F., 2004. Volcanic vent self-similar clustering and crustal thickness in the northern Main Ethiopian Rift. Geophys. Res. Lett. 31, L04604. https://doi.org/10.1029/2003GL018574.
Mazzarini, F., 2007. Vent distribution and crustal thickness in stretched continental crust: the case of the Afar Depression (Ethiopia). Geosphere 3, 152–162. https://doi.org/10.1130/GES00070.1.
Mazzarini, F., Armienti, P., 2001. Flank cones at Mount Etna volcano: do they have a power-law distribution? Bull. Volcanol. 62, 420–430. https://doi.org/10.1007/s0445000109.
Mazzarini, F., D'Orazio, M., 2003. Spatial distribution of cones and satellite-detected lineaments in the Pali Aike Volcanic Field (southernmost Patagonia): Insights into the tectonic setting of a Neogene rift system. J. Volcanol. Geotherm. Res. 125, 291–305. https://doi.org/10.1016/S0377-0273(03)00120-3.
Mazzarini, F., Isola, I., 2010. Monogenetic vent self-similar clustering in extending continental crust: examples from the East African Rift System. Geosphere 6, 567–582.
Mazzarini, F., Isola, I., 2021. Vent distribution and structural inheritance in an embryonic rift: the example of the Chyulu Hills off-rift magmatic range (South Kenya). J. Volcanol. Geotherm. Res. 416, 107268 https://doi.org/10.1016/jvolgeores.2021.107268.
Mazzarini, F., Isola, I., 2022. Quaternary off-rift volcanism along a section of the East African Rift System (EARS), from the South Ethiopia to the South Kenya. Ital. J. Geosci. 141 (3), 334–347. https://doi.org/10.3301/IJG.2022.19.
Mazzarini, F., Fornaciai, A., Bistacchi, A., Pasquare, F.A., 2008. Fissural volcanism, Polygenetic Volcanic fields, and Crustal Thickness in the Payen Volcanic complex on the Central Andes Foreland Mendoza, Argentina. Geochem. Geophys. Geosyst. 9, Q09002. https://doi.org/10.1029/2008GC002037.
Mazzarini, F., Ferrari, L., Isola, I., 2010. Self-similar clustering of cinder cones and crust thickness in the Michoacan–Guanajuato and Sierra de Chichinautzin volcanic fields, Trans-Mexican Volcanic Belt. Tectonophysics 486, 55–64.
Mazzarini, F., Keir, D., Isola, I., 2013. Spatial relationship between earthquakes and volcanic vents in the Central-Northern Main Ethiopian Rift. J. Volcanol. Geotherm. Res. 262, 123–133.
Mazzarini, F., Le Corvec, N., Isola, I., Favalli, M., 2016. Volcanic field elongation, vent distribution, and tectonic evolution of a continental rift. The Main Ethiopian Rift example: Geosphere 12, 3, 706–720. https://doi.org/10.1130/GES01193.1.
Mège, D., Masson, P., 1996. A plume tectonics model for the Tharsis province. Mars. Planet. Space Sci. 44, 1499–1546. https://doi.org/10.1016/S0032-0633(96)00113-4.
Muirhead, J.D., Kattenhorn, S.A., Le Corvec, N., 2015. Varying styles of magmatic strain accommodation across the East African Rift. Geochemistry Geophysics Geosystems 16, 2775–2795. https://doi.org/10.1002/2015GC005918.
Nahm, A.L., Schultz, R.A., 2010. Evaluation of the orogenic belt hypothesis for the formation of the Thaumasia Highlands, Mars. Journal of Geophysical Research, Planets 115 (E04008), 2010. https://doi.org/10.1029/2009JE003327.
Nakamura, K., 1977. Volcanoes as possible indicators of tectonic stress. J. Volcanol. Geotherm. Res. 2, 1–16. https://doi.org/10.1016/0377–0273(77)90012–9.
Neukum, G., Jaumann, R., the HRSC Co-Investigator and Experiment Team, 2004. HRSC: the High Resolution Stereo camera of Mars Express. Eur. Space Agency Spec. Publ. 1240, 17–35.
Neumann, G.A., Zuber, M.T., Wieczorek, M.A., McGovern, P.J., Lemoine, F.G., Smith, D. E., 2004. Crustal structure of Mars from gravity and topography. Journal of Geophysical Research, Planets 109 (E08002), 2004. https://doi.org/10.1029/2004JE002262.
Orbach, R., 1986. Dynamics of fractal networks. Science 231 (4740), 814–819. https://doi.org/10.1126/science.231.4740.814.
Phillips, T.B., Magee, C., 2020. Structural controls on the location, geometry and longevity of an intraplate volcanic system: the Tuatara Volcanic Field, Great South Basin, New Zealand. J. Geol. Soc. 177, 1039–1056. https://doi.org/10.1144/jgs2020-050.
Plescia, J.B., 2000. Geology of the Uranius group volcanic constructs: Uranius Patera, Ceraunius Tholus, and Uranius Tholus. Icarus 143, 376–396. https://doi.org/10.1006/icar.1999.6259.
Pozzobon, R., Mazzarini, F., Massironi, M., Marinangeli, L., 2015. Self-similar clustering distribution of structural features on Ascraeus Mons (Mars): implications for magma chamber depth. Geol. Soc. Lond., Spec. Publ. 401 https://doi.org/10.1144/SP401.12.
Pozzobon, R., Orlandi, D., Pagli, C., Mazzarini, F., 2021. Volcano dynamics vs tectonics on Mars: evidence from Pavonis Mons. J. Volcanol. Geotherm. Res. 410, 107148 https://doi.org/10.1016/j.jvolgeores.2020.107148.
Richardson, J.A., Bleacher, J.E., Baptista, A.A.R., 2010. Identification of volcanic ridge in Northern Syria Planum, Mars: Constraint on geologic history of Syria. Lunar and Planetary Science Conference 41, 1427.
Richardson, J.A., Bleacher, J.E., Glaze, L.S., 2013. The volcanic history of Syria Planum, Mars. J. Volcanol. Geotherm. Res. 252, 1–13. https://doi.org/10.1016/j.jvolgeores.2012.11.007.
Richardson, J.A., Bleacher, J.E., Connor, C.B., Glaze, L.S., 2021. Small volcanic vents of the Tharsis Volcanic Province, Mars. Journal of Geophysical Research: Planets 126. https://doi.org/10.1029/2020JE006620 e2020JE006620.
Robbins, S.J., Di Achille, G., Hynek, B.M., 2011. The volcanic history of Mars: High-resolution crater-based studies of the calderas of 20 volcanoes. Icarus 211, 1179–1203. https://doi.org/10.1016/j.icarus.2010.11.012.
Rooney, T.O., Bastow, I.D., Keir, D., 2011. Insights into extensional processes during magma assisted rifting: evidence from aligned scoria cones and maars. J. Volcanol. Geotherm. Res. 201, 83–96. https://doi.org/10.1016/j.jvolgeores.2010.07.019.
Rossi, M.J., 1996. Morphology and mechanism of eruption of postglacial shield volcanoes in Iceland. Bull. Volcanol. 57, 530–540.
Schultz, R.A., 1998. Multiple-process origin of Valles Marineris basins and troughs. Mars. Planet. Space Sci. 46, 827–829. https://doi.org/10.1016/s0032-0633(98)00030-0.
Smith, I.E.M., Németh, K., 2017. Source to surface model of monogenetic volcanism: a critical review. In: Németh, K., Carrasco-Nunez, G., Aranda-Gomez, J.J. & Smith, I.E. M. (eds). Monogenetic Volcanism, Geological Society, London, Special Publications 446, 1–28. https://doi.org/10.1144/SP446.14.
Smith, D.E., Zuber, M.T., Frey, H.V., Garvin, J.B., Head, J.W., Muhleman, D.O., Pettengill, G.H., et al., 2001. Mars Orbiter Laser Altimeter—Experiment summary after the first year of global mapping of Mars. J. Geophys. Res. 106 (E10), 23689–23722. https://doi.org/10.1029/2000JE001364.
Song, C., Havlin, S., Makse, H.A., 2005. Self-similarity of complex networks. Nature 433, 392–395. https://doi.org/10.1038/nature03248.
Spörli, B.K., Eastwood, V.R., 1997. Elliptical boundary of an intraplate volcanic field, Auckland, New Zealand. J. Volcanol. Geotherm. Res. 79 (3–4), 169–179. https://doi.org/10.1016/S0377-0273(97)00030-9.
Stauffer, D., Aharony, A., 1994. Introduction in Percolation Theory, revised second edition. CRC Press, Washington D.C., p. 181
Tadini, A., Bonali, F.L., Corazzato, C., Cortés, J.A., Tibaldi, A., Valentine, G.A., 2014. Spatial distribution and structural analysis of vents in the Lunar Crater Volcanic Field (Nevada, USA). Bull. Volcanol. 76, 877. https://doi.org/10.1007/s00445-014-0877-8.
Takada, A., 1994. The influence of regional stress and magmatic input on styles of monogenetic and polygenetic volcanism. J. Geophys. Res. 99 (B7), 13563–13573.
Tanaka, K.L., Robbins, S.J., Fortezzo, C.M., Skinner, J., Hare, T.M., 2014. The digital global geologic map of Mars: Chronostratigraphic ages, topographic and crater morphologic characteristics, and updated resurfacing history. Planet. Space Sci. 95, 11–24. https://doi.org/10.1016/j.pss.2013.03.006.
Tibaldi, A., 1995. Morphology of pyroclastic cones and tectonics. J. Geophys. Res. 100 (B12), 24,521–24,535.
Torson, J.M., Becker, K.J., 1997. ISIS - a software architecture for processing planetary images. Lunar Planet. Sci. Conf. 28, 1219.
Walsh, J.J., Watterson, J., 1993. Fractal analysis of fracture pattern using the standard box-counting technique: valid and invalid methodologies. J. Struct. Geol. 15, 1509–1512.
Werner, S.C., 2009. The global martian volcanic evolutionary history. Icarus 201, 44–68. https://doi.org/10.1016/j.icarus.2008.12.019.
Wilson, L., Head, J.W., 2002. Tharsis-radial graben systems as the surface manifestation of plume-related dike intrusion complexes: Models and implications. J. Geophys. Res. 107 (E8), 5057. https://doi.org/10.1029/2001JE001593.
Yin, A., 2012. Structural analysis of the Valles Marineris fault zone: possible evidence for large-scale strike-slip faulting on Mars. Lithosphere 4 (4), 286–330. https://doi.org/10.1130/L192.1.
Zuber, M.T., 2001. The crust and mantle of Mars. Nature 412, 220–227.
Zuber, M.T., et al., 2000. Internal Structure and early thermal Evolution of Mars from Mars Global Surveyor Topography and Gravity. Science 287, 1788–1793. https://doi.org/10.1126/science.287.5459.1788.